# Bio-inspired kinematical control of redundant robotic manipulators

*Ali Leylavi Shoushtari and Stefano Mazzoleni*
Institute of BioRobotics, Scuola Superiore Sant'Anna, Pontedara, Italy, and
Laboratory of Rehabilitation Bioengineering, Auxilium Vitae Rehabilitation Centre, Volterra, Italy, and
*Paolo Dario*
Institute of BioRobotics, Scuola Superiore Sant'Anna, Pontedara, Italy

**Abstract**

**Purpose** – This paper aims to propose an innovative kinematic control algorithm for redundant robotic manipulators. The algorithm takes advantage of a bio-inspired approach.

**Design/methodology/approach** – A simplified two-degree-of-freedom model is presented to handle kinematic redundancy in the x-y plane; an extension to three-dimensional tracking tasks is presented as well. A set of sample trajectories was used to evaluate the performances of the proposed algorithm.

**Findings** – The results from the simulations confirm the continuity and accuracy of generated joint profiles for given end-effector trajectories as well as algorithm robustness, singularity and self-collision avoidance.

**Originality/value** – This paper shows how to control a redundant robotic arm by applying human upper arm-inspired concept of inter-joint dependency.

**Keywords** Robotics, Redundancy, Motion control, Geometric algorithm, Joint angles synergy, Motion planning

**Paper type** Research paper

## 1. Introduction

Numerous instances of redundancy can be found in biological and artificial systems. One of the most significant is represented by the musculoskeletal structure of human body which can be modeled as a kinematic chain (Khatib *et al.*, 2009). Maneuverability is a consequential feature which allows redundant systems to have dexterous behavior, e.g. manipulation. Mechanisms with redundant degrees of freedom (DOFs) are potentially able to perform dexterous tasks. Although redundancy provides maneuverability in terms of efficiency, on the other hand, it also raises problems in the motion planning.

Over the past decades, a growing attention has been paid to redundant robotic manipulators because of the several advantages linked to the exploitation of redundancy, such as safety and maneuverability. Despite them, redundancy is often considered as a problem from the control point of view. Several resolutions have been presented to deal with that in position (Seraji, 1989; Chang, 1987), velocity (Whitney, 1969; Yoshikawa, 1985) and acceleration (Hollerbach and Suh, 1987) levels. These solutions fall in three main categories: linear algebra-based (LAB), soft computing-based (SCB) and bio-inspired approaches (BIO).

The pseudo-inverse is a fundamental method in the LAB category Siciliano (1990) which proposes to decouple the joint velocities into two terms associated with the operational space and the null space (Whitney, 1969, 1972). The second component usually is subjected for optimizing a arbitrary criterion. The main advantage of this method is to provide a possibility to incorporate a biological-based defined criterion as second term, e.g. collision avoidance(Maciejewski and Klein, 1985), minimum joint torques (Chen *et al.*, 1994) and task priority (Chiaverini, 1997; Nakamura *et al.*, 1987).

The SCB approaches including artificial neural networks (pseudo-inverse network Wang, 1997 and linear programming neural networks Xia, 1966), fuzzy logic (Ramos and Koivo, 2002) and genetic algorithms generally rely on linear algebraic equations presented in the previous category; consequently, the invertibility of the Jacobian matrix which occurs in singular/near singular points represents an issue to be considered.

The BIO methods are third category of redundancy resolutions where the specific strategies that human central nervous system (CNS) uses to control body movements are considered as source of inspiration. The majority of human imitation-based motions planning techniques are based on directly mimicking the human arm posture Kim *et al.* (2005)

The current issue and full text archive of this journal is available on Emerald Insight at: **www.emeraldinsight.com/0144-5154.htm**

Assembly Automation
36/2 (2016) 200–215
© Emerald Group Publishing Limited [ISSN 0144-5154]
[DOI 10.1108/AA-11-2015-116]

This work was partly funded by Centro di Riabilitazione Motoria INAIL, Volterra, Italy (Research project "Design, development, validation and clinical experimentation of a robotic device for verticalisation and mobility of persons affected by severe motor disabilities", 2013-2015).

Received 30 November 2015
Revised 29 December 2015
Accepted 1 January 2016

and hand pose Pollard *et al.* (2002) (position and orientation). In fact, these methods, known as bio-mimetic approaches, try to imitate the human arm movement Potkonjak *et al.* (1998), Caggiano *et al.* (2006) for robotic motion planning purposes. The task-specification represents the main feature of these approaches, restricting their motion planning capability on the tasks where the data sets were recorded from. In other words, in addition to the ability to generate human-like motion, the generalization should also be considered as a mandatory property of a kinematic control for anthropomorphic manipulators.

Contrary to imitation-based approaches, the other BIO methods put emphasis on human movement primitives (Abedi and Leylavi Shoushtari, 2012). These methods try to solve kinematic redundancy in human-like fashion by means of satisfying biological-based defined constraints/cost functions (Abedi and Leylavi Shoushtari, 2012). In particular, human motion principles, e.g. metabolic energy consumption Cruse *et al.* (1990) and postural stability Leylavi Shoushtari (2013), are designed as cost functions which are subjected to be minimized by an optimal motion planning algorithm. Complexity and difficulty-to-generalization represent their main deficiencies.

Visuo-motor coordination neural models of humans Asuni *et al.* (2003) and specific learning ability are another motion principles where Guglielmelli *et al.* (2006) represented a neurocontroller to control a redundant manipulator. With respect to the nature of the learning which occurs within an action–perception cycle, the previously mentioned controller was developed to a model-free learning-based framework to control the pose of the end effector of a redundant robotic arm (Asuni *et al.*, 2006). The same work with capability of fast response and learning ability through experiments was proposed by Qiao *et al.* (2015).

The concept of synergy was implemented in analysis complex motor behavior of human and animals (Santello *et al.*, 1998; Torres-Oviedo *et al.*, 2006). Nowadays, joint synergy-based approach is being considered as another BIO redundancy solution aimed to identify a motion planning algorithm that does not only relies on limited set of captured data but also can be generalized to unknown motion. In particular, the motor synergies have been proposed to deal with redundancy in modeling human grasping Santello *et al.* (1998) and human-liked motion planning for robotic hands(Palli *et al.*, 2014). Suarez *et al.* (2015) proposed a synergy-based approach for dual-arm manipulation which is capable to extract the human motion principles and incorporate them in motion generation of a robotic system. To approach human-like motion planning, generalization is a key feature; accordingly, Artemiadis *et al.* (2010) tried to encode the anthropomorphic characteristics of human upper arm motion in a mathematical function and then incorporated the model in an inverse kinematic resolution. In fact, they used a Bayesian network to extract the inter-joint dependencies and then they formulated the dependencies as an objective function to be implemented in a closed-form inverse kinematic algorithm. The algorithm was successful in generating bio-mimetic motion, and it could also develop new anthropomorphic motions, not previously seen in captured-motions set. The main limitation of this method is its reliability on the Jacobian-based inverse kinematic resolution which would not work in singular/near singular points.

**Figure 1 (a)** Schematic configuration of the mechanism with n DOFs and **(b)** simplified model of the redundant mechanism with 2 DOFs. $\mathbf{q_1}$, $\mathbf{q_2}$ are the generalized coordination of prismatic and revolute joints, respectively

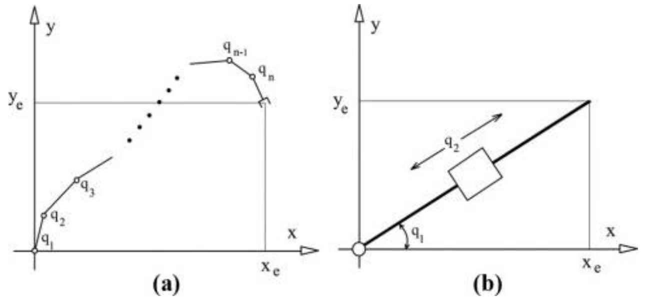

**Figure 2** The unified computational framework for motion planning of a 4 DOFs robot manipulator. The $\boldsymbol{\lambda_r}$ is real value of the rotational variable calculated for the robot end-effector and $\boldsymbol{\Delta\lambda}$ is the compensation term for the first joint

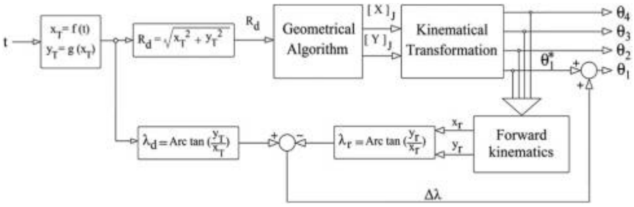

The concept of postural synergies previously was used to explain how the human CNS controls the complex/redundant

**Figure 3** The morphology of the robot is considered as a second order polynomial curve controlled by two main parameters **k** and **R**

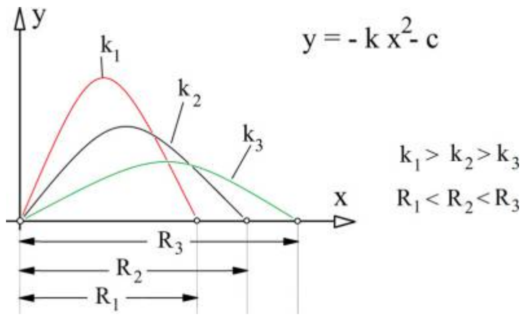

**Figure 4** The geometric algorithm as a control loop to calculate the Cartesian position of the robot's joints

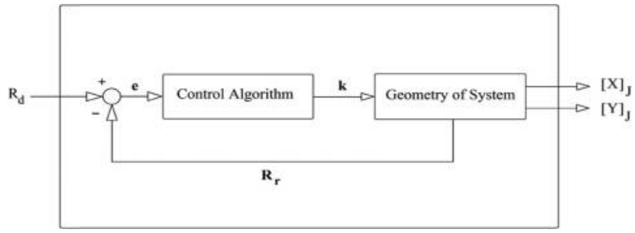

**Figure 5** The computational geometric algorithm designed to calculate the Cartesian position of the joints and the real radial distance $\mathbf{R_r}$ based on input **k** together with the knot vector $\mathbf{X_{knot}}$. $\mathbf{X_{knot}}$ is vector of five points evenly distributed between the two roots of the parabola (it is illustrated in the top-left box of this figure)

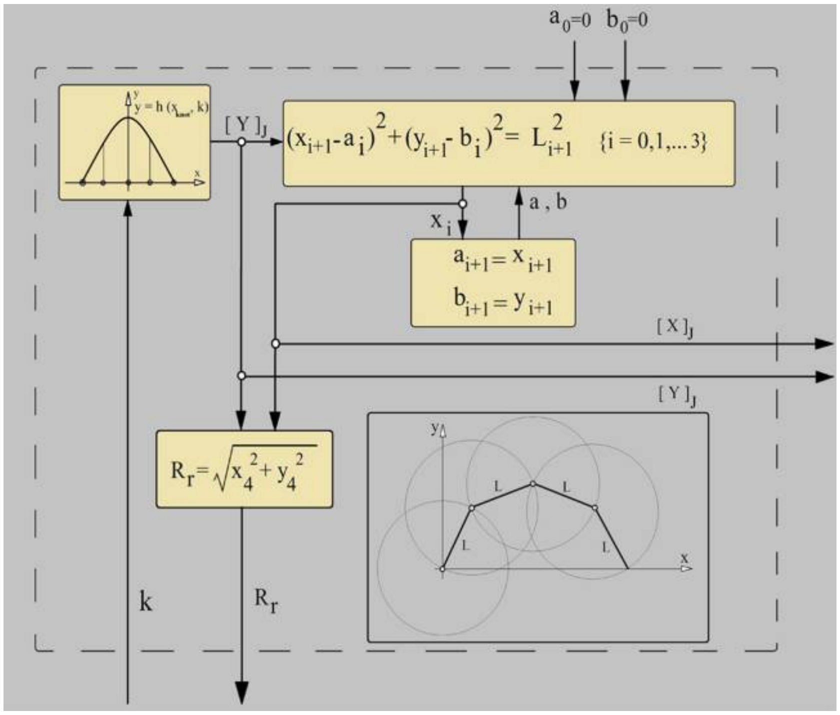

kinematical structure of the human hand during grasping task (Santello *et al.*, 1998). In this study, we take advantage of this biologically inspired concept to present a motion planning approach for redundant manipulators. The proposed approach takes advantage of a 2-DOF simplified model and a novel servo mechanism (to be presented in Section 2, Subsection 2.1

**Figure 6** The control algorithm designed to regulate the **k** value to reach $\mathbf{e = E_a}$

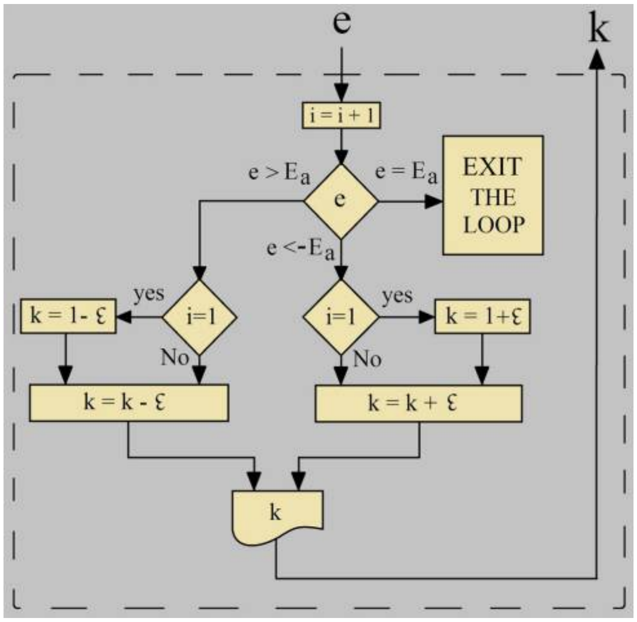

**Table I** RMSE, computation time and minimum acceptable error as result of simulation with optimal step size and optimal MAE

| Trajectory | Optimal $\varepsilon$ | Optimal MAE (m) | RMSE (m) | CTSP (ms) |
|---|---|---|---|---|
| **Polynomial** | $3.75 \times 10^{-4}$ | $4.50 \times 10^{-4}$ | 0.0133 | 5.06 ± 0.12 |
| **Circular** | $4.69 \times 10^{-4}$ | $1.00 \times 10^{-4}$ | 0.0012 | 18.02 ± 0.68 |
| **P-shape** | $5.4 \times 10^{-4}$ | $4.00 \times 10^{-4}$ | 0.0019 | 4.93 ± 0.41 |
| **Elliptic** | $4.06 \times 10^{-4}$ | $3.20 \times 10^{-4}$ | 0.0019 | 15.97 ± 0.52 |
| **Oval spring** | $7.5 \times 10^{-4}$ | $1.47 \times 10^{-4}$ | 0.00006 | 19.53 ± 0.13 |

**Figure 7** The predicted postures of the redundant robot. Black line represents the path of the end-effector, red square corresponds to the position which is selected based on random values of **k** and $\boldsymbol{\lambda}$.

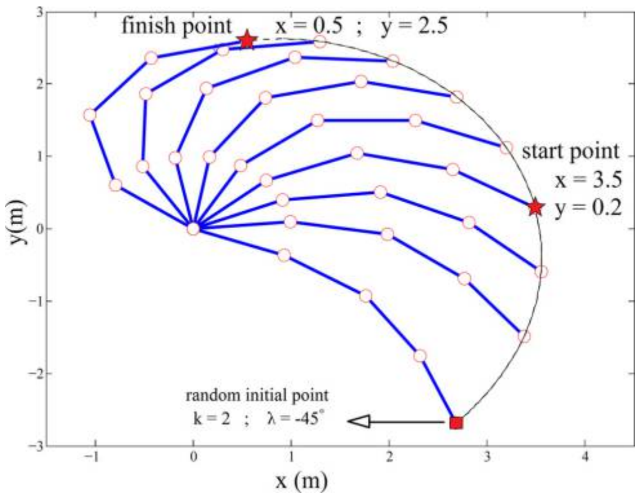

**Figure 8** The predicted postures for three paths

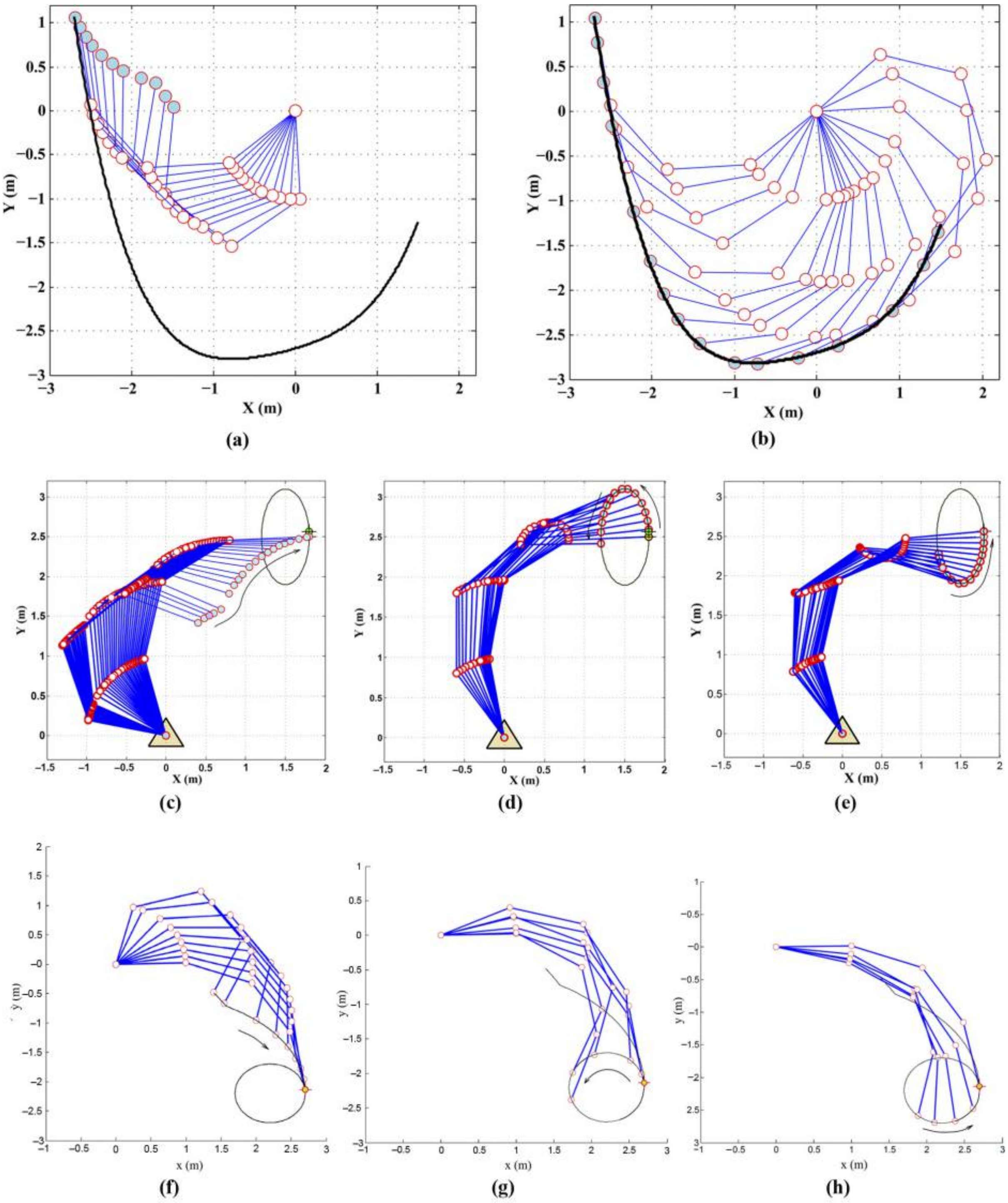

**Notes:** (a)-(b): The generated motion for the polynomial path; (c)-(e): the generated motion for the elliptic path; (f)-(h): the generated motion for the circular path

Geometric algorithm) to generate motion for redundant robotic manipulators. The main advantage of this algorithm is to be Jacobian-free: singular/near singular points will not represent a problem anymore. First, the redundant mechanism is modeled as a system with two DOFs considering a prismatic and revolute joint regardless of the numbers of DOFs. The geometry of the robot's workspace is formulated in polar coordination using linear and rotational displacement. A joint synergy is designed in a way that forms the configuration of robot as a parabola. So that, the linear distance could be regulated by adjusting the curvature.

In the second section, the unified framework used for the motion planning is introduced. Third section describes a geometric algorithm which consists of two separate subparts: "control algorithm" and "geometry of system". As results, four sample end-effector trajectories are designed, and their relevant joint profiles are generated using the proposed geometric algorithm. Then the three-dimensional extension of this approach will be presented.

## 2. Unified motion planning framework

The simplified 2-DOF mechanism is presented as the model of a planar redundant robot ($q_1$ and $q_2$ are the DOFs shown in Figure 1(b)). The algorithm presented in Figure 2 uses $x_T$ and $y_T$ as time-dependent variables of Cartesian position of end effector and then it transforms these variables to polar coordination $R_d$ and $\lambda_d$. These parameters are equivalents of $q_1$ and $q_2$ represented in Figure 2. Actually, $R_d$ and $\lambda_d$ are distance and angle of the target point respect to the base of robot, respectively. Then, the *geometrical algorithm* calculates the Cartesian positions of joints. Joint positions are a set of the postures of robot to reach the target point. The $[X]_j$ and $[Y]_j$ are vectors of joint positions defined according to equation (1). The $x_i$ and $y_i$ are horizontal and vertical position of $i^{th}$ joint, respectively.

The kinematical transformation translates the joint variable from workspace into joints space. Finally, λ is added to the angle of the first joint to locate the end effector at the target point position. The joint angles are regulated to adjust radial distance $R_d$ and after that the first joint angle is also adjusted by adding λ:

$$[X]_j = [x_1 x_2 x_3 \ldots x_n];\ [Y]_j = [y_1 y_2 y_3 \ldots y_n] \qquad (1)$$

### 2.1 Geometric algorithm

The central part of this paper deals with the geometric-based computational algorithm which calculates the Cartesian positions of joints. The main idea of the proposed algorithm is to control the robot posture to reach the target point.

Let us assume that a planar redundant robot is configured in a parabolic posture. Given $k$ as the coefficient of the formulation of this curve and $R$ as the distance between its roots, an inverse relation between $k$ and $R$ can be found with respect to the Figure 3. In fact, this figure shows that increasing coefficient $k$ causes the reduction of $R$. The main idea is to regulate the coefficient $k$ to reach to desired radial distance $R$. The error signal $e$ is computed as difference between the real and the desired distances, $R_r$ and $R_d$, respectively.

The control algorithm uses the $e$ to regulate the control variable $k$ to set the end effector on the target point. Then this value is used by a computational algorithm to calculate the vertical and horizontal position of joints. The closed loop system is designed to regulate the posture of robot to reach to desire distance $R_d$ (Figure 4).

### 2.2 Geometry of system

A second-order polynomial function $h(x_{knot}, k)$ is implemented to calculate the vertical position of the joints. In fact, the $k$ value would determine the curvature of the parabola, while the knot vector of $x_{knot}$ provides preliminary horizontal position. Later on, the resulted vertical position of joints $[Y]_J$ is integrated in geometric model of a redundant planar robot (illustrated in bottom right box of Figure 5) to calculate horizontal position of joints $[X]_J$. This geometry takes

**Figure 9** The simulation results of P-shape trajectory tracking (4 DOFs). The predicted postures are shown in **(a)–(e)**

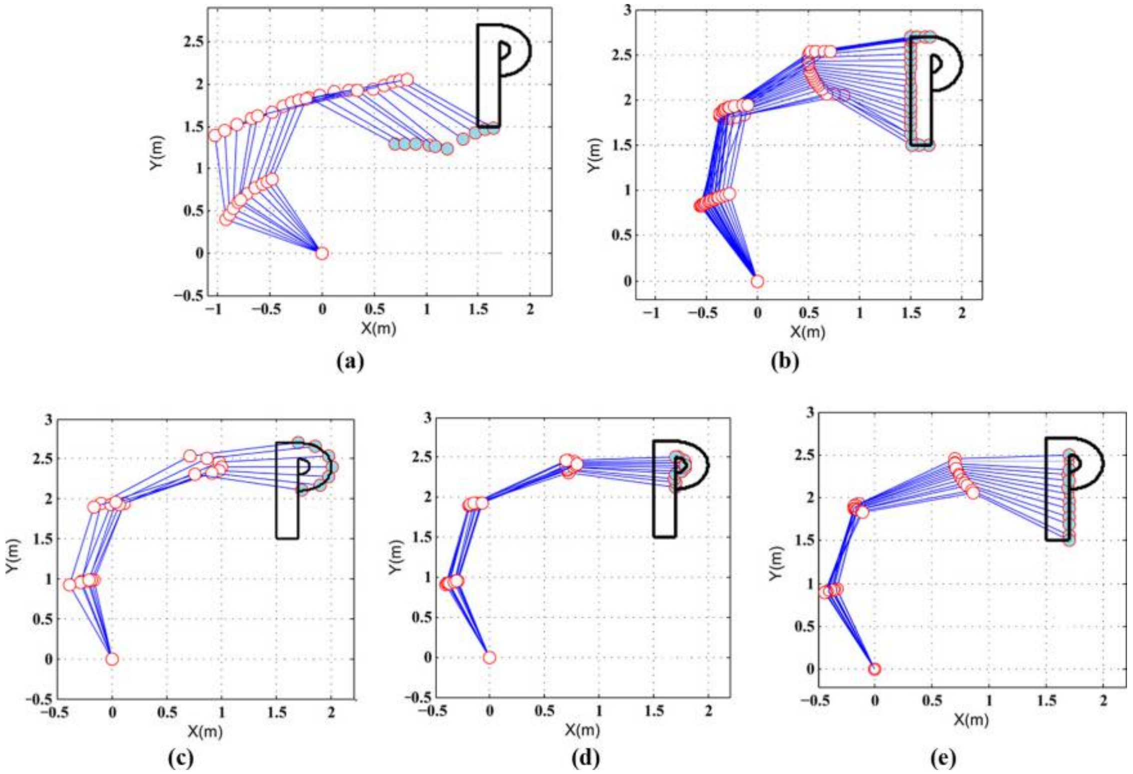

advantage of the equation of a circle to describe the *locus* of the tip of the each link. To understand it better, let us consider the joint as located at the center of a circle, so the position of tip of the link could be described by the equation of circle with diameter as long as length of the link.

In equation (2), $x_{i+1}$ and $y_{i+1}$ are the horizontal and vertical position of the end of the (i + 1)th link, respectively, $a_i$ and $b_i$ are the horizontal and vertical position of joint of (i + 1)th link, respectively. The $L_{i+1}$ is the length of the (i + 1)th link. By using this equation and considering $a_0 = 0$, $b_0 = 0$ (as the position of the first joint) and using $y_1$ which is calculated from "control algorithm" section, $x_1$ is calculated. Based on a recursive method shown in Figure 5, the $x_2$, $x_3$, $x_4$ are obtained. Figure 5 also illustrates this recursive algorithm to calculate the vertical and horizontal position of joints based on a given k value:

$$(x_{i+1} - a_i)^2 + (y_{i+1} - b_i)^2 = L_{i+1}{}^2 \qquad (2)$$

### 2.3 Control algorithm

Figure 6 depicts how the control algorithm computes the *k* value for a given error *e*. For a negative error, the *k* initiates with a value greater than 1, and for the positive error, *k* initiates with the value between 0 and 1. $\varepsilon$ denotes step size used to increase or decrease the *k* value and the *i* is counter variable of the loop. $E_a$ is the acceptable error: it has a positive value defined in Table I.

## 3. Simulation of planar task

The foregoing algorithm is used for point-to-point motion planning, in fact, any given trajectory must be divided into control points: the approach aims to predict the motion between every two control points. A 4-DOF planar robot manipulator is considered for point-to-point motion planning task. Each of the four links is 1-m length. Three different sample trajectories are used for validation purposes. For each

**Figure 10** End-effector tracking error during polynomial, circular,P-shape and elliptic trajectory tracking (top to bottom)

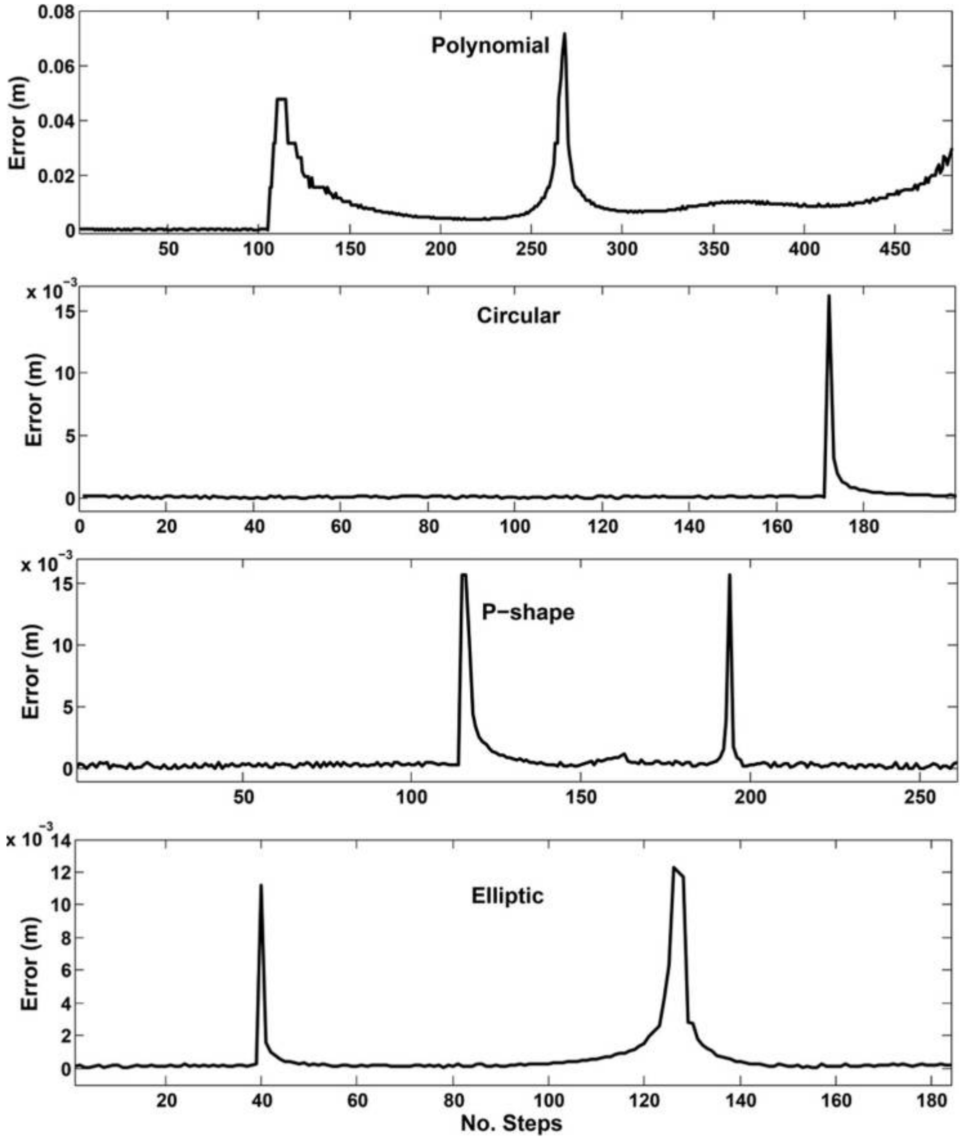

trajectory, the motion initiates from a random position indicated by random values of $k$ and λ, and it continues till reaching the starting point. The end effector starts motion from initial point and locates at final position in times $t = 0$ and $t = T$, respectively.

Figure 7 shows the predicted path and postures from a random initial position to the starting point and from the starting point to the final position indicated by red squares and red stars, respectively. The random initial points are generated using the angle λ and the desired radial distance $R_d$ obtained from parameter $k$ (Figure 3).

The algorithm generates the end-effector path and joints position of the robot to move the end effector between the given initial and final points. Three continuous trajectories have been simulated and tested to show the algorithm performance for open or closed paths.

The first sample trajectory is represented by a fourth-order polynomial curve for interval $x \varepsilon [-2.4, 1.5]$ defined by (3). The considered path of the end effector is digitized to control points and then the algorithm is integrated to predict the path and postures between every two points. Figure 7 shows predicted postures of the 4-DOF redundant robot manipulator. Four sample trajectories were selected to validate the control algorithm: polynomial, elliptic, circular and "P"-shape trajectory. Trajectory (1) (top row plots in Figure 8) was computed as follows:

$$y = -2.7 + 0.27x + 1.5x^2 + 0.07x^3 + 0.09x^4 \qquad (3)$$

The initial position is chosen randomly based on random k and λ values as mentioned before. Top row plots in Figure 8 illustrate the predicted motion of the robot following polynomial trajectory. The elliptic trajectory (middle row plots in Figure 8) was computed according to equation (4). It represents a circle with 0.5-m radius whose center is located at (2.2 m, −2.2 m):

$$\frac{(x - 1.5)^2}{0.09} + \frac{(y - 2.5)^2}{0.36} = 1 \qquad (4)$$

The circular trajectory (bottom row plots in Figure 8) corresponds to a circular path computed according to equation (5) whose radius is 0.5 m and center located at (2.2 m, −2.2 m):

$$(x - 2.2)^2 + (y + 2.2)^2 = 0.25 \qquad (5)$$

The trajectory presented in Figure 9 corresponds to the shape of the letter "P". The trajectory consists of straight lines (B and E), curves (C and D) and Section A positioning on start point.

Figure 10 shows the tracking error for the mentioned paths. The error is calculated as horizontal and vertical deviation of the predicted position ($x_p$, $y_p$) from the desired trajectory ($x_d$, $y_d$) according to equation (6):

$$Error = \sqrt{(y_d - y_p)^2 + (y_d - y_p)^2} \qquad (6)$$

Here we introduce the "Optimal Point Analysis" method which is used to find optimal value for the critical parameters of the algorithm. These parameters are "Step Size" and "Acceptable Error" which represent the performance indicators for algorithm's *speed* and *accuracy*, respectively. As these factors have opposite trends, the maximum efficiency is usually achieved just by finding a trade-off between speed and accuracy. Accordingly, we define the algorithm's optimal point as an amount of *step size* and *acceptable error* which leads to achieve highest computational speed and accuracy at the same time. To reach this goal, we applied the algorithm to analyze the optimal point illustrated by Figure 11.

The calculated normalized root mean square error (NRMSE) and normalized computational time for single point (NCTSP) are plotted against step size ε (for the ten values) and four trajectories (Figure 12). As expected, decreasing the resolution of the algorithm (by increasing step size) leads to the decreasing accuracy and increasing computation speed. Hence, the optimal algorithm resolution ε is obtained through making a trade-off between NRMSE and NCTSP. Accordingly, the intersection of these two graphs gives optimal ε which, by using the minimum acceptable error (MAE) and ε diagram (Figure 13), will also give−the optimal MAE. The optimal values of MAE and ε used to generate the motion for the four trajectories are shown in Table I.

## 4. Spatial motion planning algorithm

### 4.1 End-effector 3D positioning

In this section, we discuss how to use the proposed algorithm to control a 7-DOF anthropomorphic robotic manipulator during a three-dimensional task. The presented motion planning approach creates a single 2D arm flexion which has effect on the planar motion of the end effector. To create a

**Figure 11** Optimal point analysis flowchart

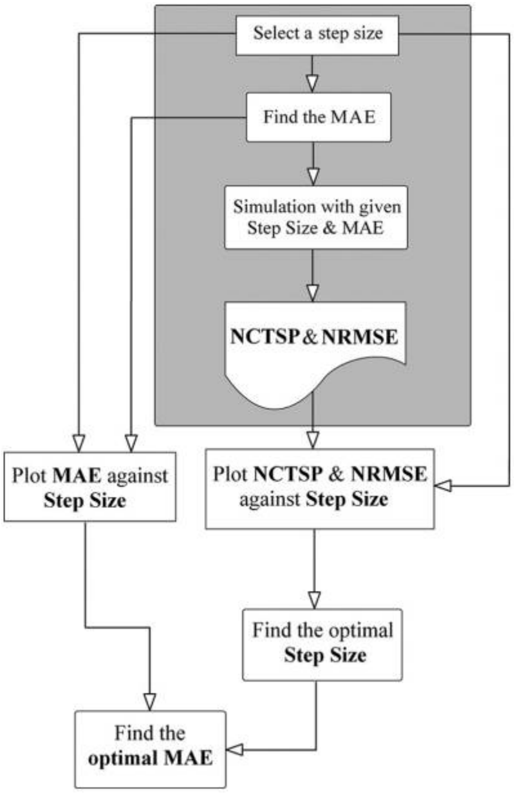
Select a step size
Find the MAE
Simulation with given Step Size & MAE
NCTSP & NRMSE
Plot MAE against Step Size
Plot NCTSP & NRMSE against Step Size
Find the optimal Step Size
Find the optimal MAE

**Figure 12** Normalized RMSE (NRMSE) and normalized computational time for single point (NCTSP) on primary and secondary vertical axes respectively, step size on the horizontal axis. The intersection points shown by stars indicate the optimal step size

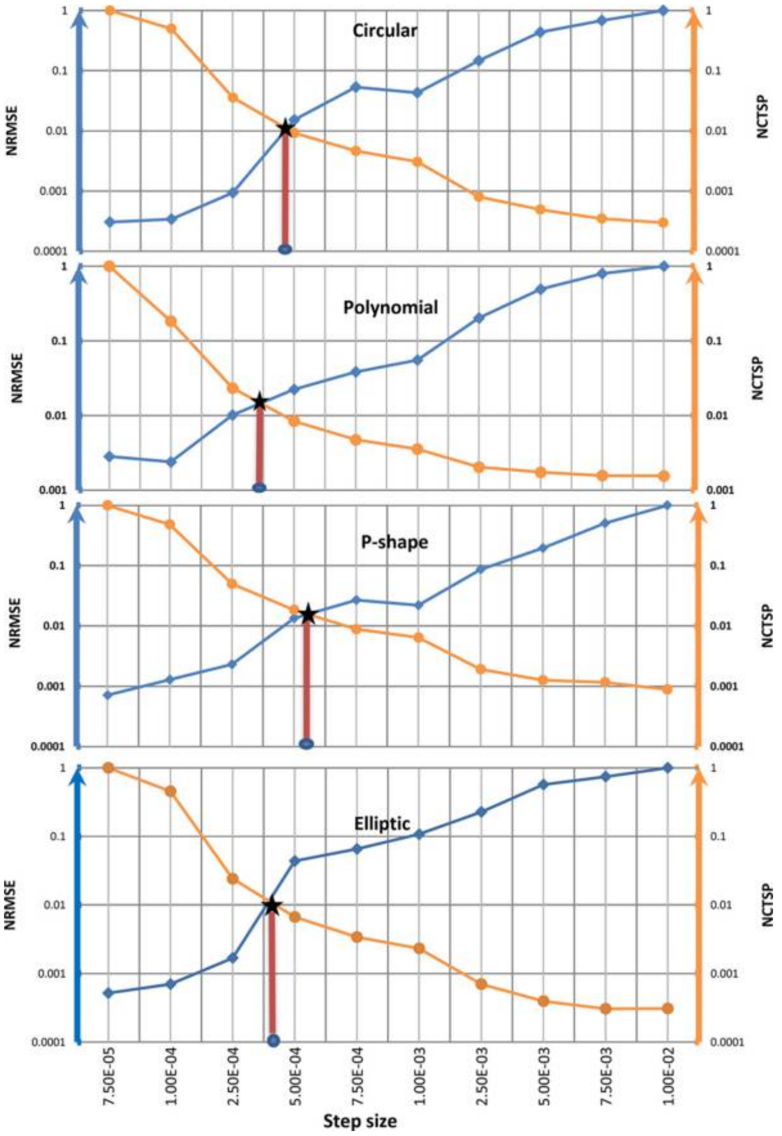

**Figure 13** MAE plotted versus algorithm step size

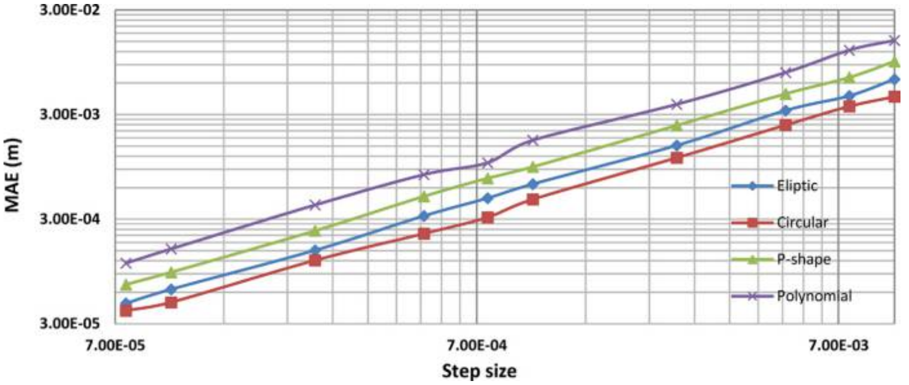

spatial positioning (for end effector), we need more than one planar motion so that we propose two separate joint synergies in which each one creates a single planar motion. Consequently, by the combination of two planar motions, we would have a spatial motion of the end effector. Each synergy is controlled by the planar motion planning algorithm presented in the previous section.

The anatomy of human arm movements is described by three pairs of terms: supination/pronation, felction/extension and abduction/adduction. In this part, we present a pair of synergies which allows the anthropomorphic robotic manipulator to mimic the first two movements of the human arm. In particular, the first synergy is in charge of controlling the arm bending in the u-w plane (Figure 14 (b)) by means of control over even joints which resemble human arm flexion/extension. The second synergy is used to create an axial torsion among whole arm in u-v plane (Figure 14 (c)) via controlling the odd joints. This motion look likes human arm supination/pronation (Figure 14 (c)). Consequently, the combination of these two synergies will lead to achieve a generic spatial positioning of the end effector (Figure 14 (d)). A three-dimensional motion is achieved by combining two 2D motions: the following section describes the control of the three-dimensional motion.

### 4.2 Modeling and motion control

To control the end-effector position, a cylindrical coordination is considered (Figure 15 (b)). The height of the cylinder is controlled by a second joint, while the alpha angle would be adjusted by the first joint.

**Figure 15** The 3DOFs cylindrical model. $\mathbf{X_E}$ is the position of the end-effector described by $\boldsymbol{\alpha}$, **h** and **r**. The control variables $\boldsymbol{\alpha}$ and **h** are regulated respectively by the angles of first and second joint ($\boldsymbol{\theta_1}$ and $\boldsymbol{\theta_2}$) while the third control variable (**r**) is adjusted by rest of the joints ($\boldsymbol{\theta_3}$-$\boldsymbol{\theta_7}$)

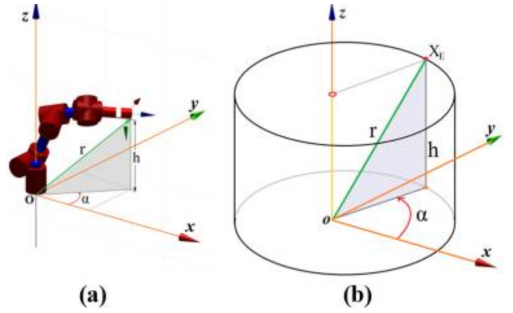

The length r is regulated by the combination of two synergies. The r value is regulated by changing the *k* value of synergies and then the height of the target point is compared with the height of the end effector. After this, the error angle for the second joint is calculated (to compensate the distance between the height of end effector and the height of the target point) and then the error angle of the first joint is defined as the difference between the alpha angle of the target point and the end effector. In each iteration, by adding these two

**Figure 14** The top row shows an anthropomorphic 7DOFs robotic manipulator controlled by joint synergies and lower row illustrates the equivalent of the whole arm motion

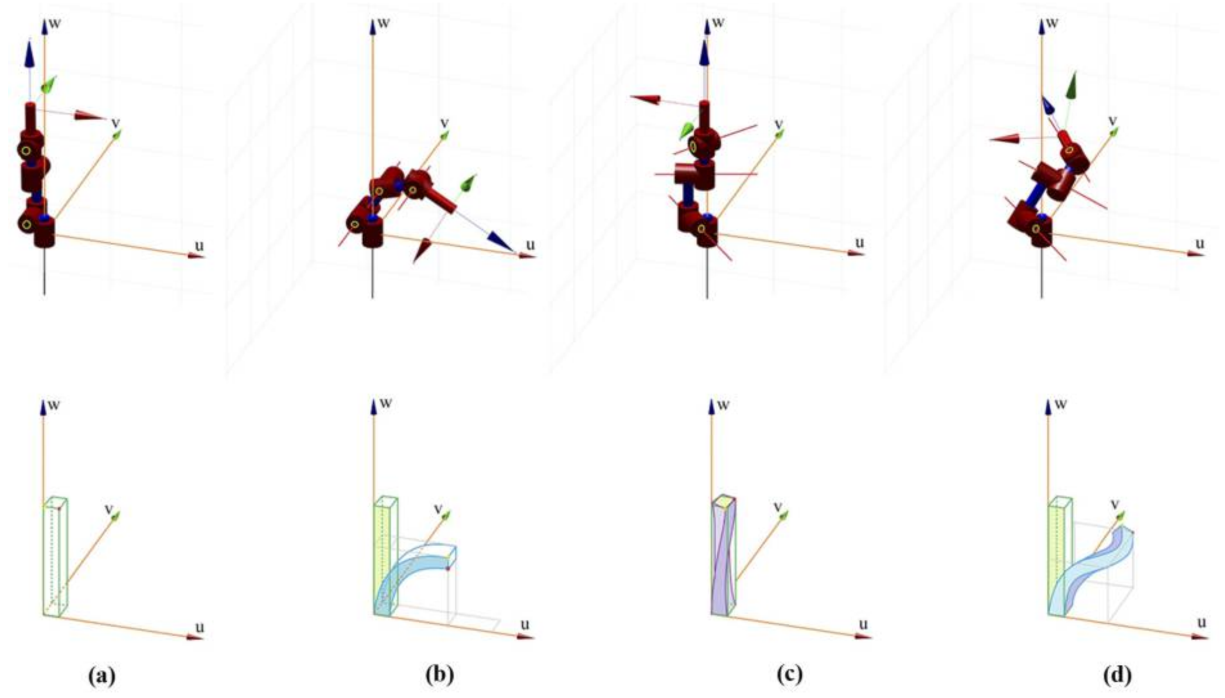

**Notes:** (a) Robotic arm in neutral position; (b) single planar bending in the uw plane; (c) torsion in the uv plane through activation of odd joints (1st, 3rd , 5th and 7th ) through activation of even joints (2nd 4th and 6th ); (d) combination of whole arm torsion and bending

**Figure 16** Block-diagram representation of the spatial motion planning algorithm. It consisted of controller (on top) and a feedback/compensatory part on bottom

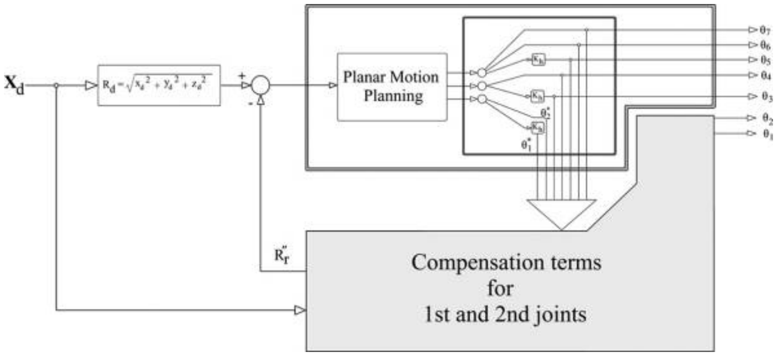

**Figure 17** Scheme of planar motion planning algorithm presented in figure 16. The parameters $\mathbf{q_1}$, $\mathbf{q_2}$ and $\mathbf{q_3}$ are the predicted angles and **e** is the error signal of vector **R** ($\mathbf{e = R_d - R_r''}$)

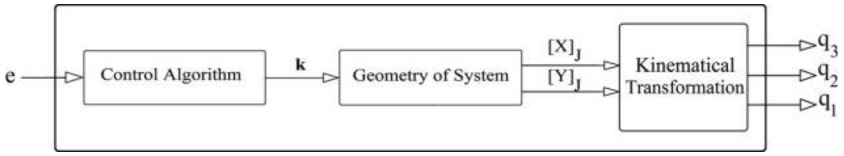

compensation terms to the predicted joint angle, the end effector may be aligned across the target point.

The entire control model consists of a controller and a feedback/compensatory compartments (Figure 16). The controller section includes a planar motion planning algorithm which is cascaded with two set of synergies. The planar motion planning block presented in Figure 16 is the same as the geometric algorithm shown in Figure 4 where the inner feedback is replaced by an external feedback loop. It generates joint angles for a planar 3-DOF model then the synergies feed the angles to odd and even joints (Figure 17). Considering red dots on the top corner of bar in Figure 14 (b and c), intuitively, we can see that the bending has a greater contribution in red dot displacement than torsion. We can apply the same observation to the robotic arm and conclude that the joints which create bending have a higher contribution in the end-effector motion. Hence, the even joints receive a greater coefficient than odd joints.

The feedback/compensatory section is designed to correct the first and second joint angle to regulate control variables α and h (presented in Figure 15) and also provides a feedback for the controller section. The feedback block also provides the $R''_r$ value which represents the real position of the end effector when it is aligned with target point. This value is implemented to calculate the position error of the end effector which is the input of planar motion planning block. The compensatory part receives the predicted joint angles from the output of synergies and calculates the required angles for the first and second joint to locate end effector at the height $h_d$ and angle $\alpha_d$ (Figure 18, top).

To achieve this goal, we first assume that the joints are fixed except of the second joint. In this situation, the trajectory of the end effector is represented by a circle in the xz plane (blue circle in Figure 18 (b)). Hence, by regulating the $\theta_2$, the height of the end effector would vary in xz plane. Considering the block diagram in Figure 18, it first solves the forward kinematic to obtain the current position of the end effector $X_r$ and then it exploits equations (7)-(11) for calculating the angles $\beta_d$ and $\beta_r$. Finally, by adding the differential value Δβ to the current angle of the second joint, the end effector is located at the desired height $h_d$. The next step is aimed to regulating the angle $\theta_1$ to relocate the end effector from $\alpha'_r$ to $\alpha_d$ where it would align with the target point. The new position of the end effector $X'_r$ is obtained by solving the forward kinematics for the current joint angles (considering the updated value for second joint $\theta_2$). Assuming that all joints except for the first are fixed, the trajectory of the end effector is represented by the circle (violet line in Figure16 (c)). To be aligned with the target point $X_d$, it just required to reach the green point which is achieved by rotating the first joint as Δα. The new position of the end effector $X''_r$ is closer to the target point. The next step is to achieve the target point by increasing/decreasing the length of $\overrightarrow{AX_r}$ vector which is carried out by the controller:

$$\overrightarrow{AX_r} = \overrightarrow{OX_r} - \overrightarrow{OA} \tag{7}$$

$$\overrightarrow{AX_d} = \overrightarrow{OX_d} - \overrightarrow{OA} \tag{8}$$

$$h_r = z_{\overrightarrow{AX_r}} \tag{9}$$

$$h_d = z_{\overrightarrow{AX_d}} \tag{10}$$

$$R_{xz} = \sqrt{x_{\overrightarrow{AX_r}}^2 + z_{\overrightarrow{AX_r}}^2} \tag{11}$$

### 4.3 Spatial motion simulation results

We designed an oval spring-form trajectory defined by (12) for end effector and then analyzed the optimal point of the algorithm for this trajectory (Figure 19). Figure 20 illustrates

**Figure 18** The top part shows the block "Compensation terms for first and second joints" presented in Figure 16. The algorithm receives joint angles $\boldsymbol{\Theta}$ and target position $\boldsymbol{X_d}$ as inputs and calculates the angles of first and second joints

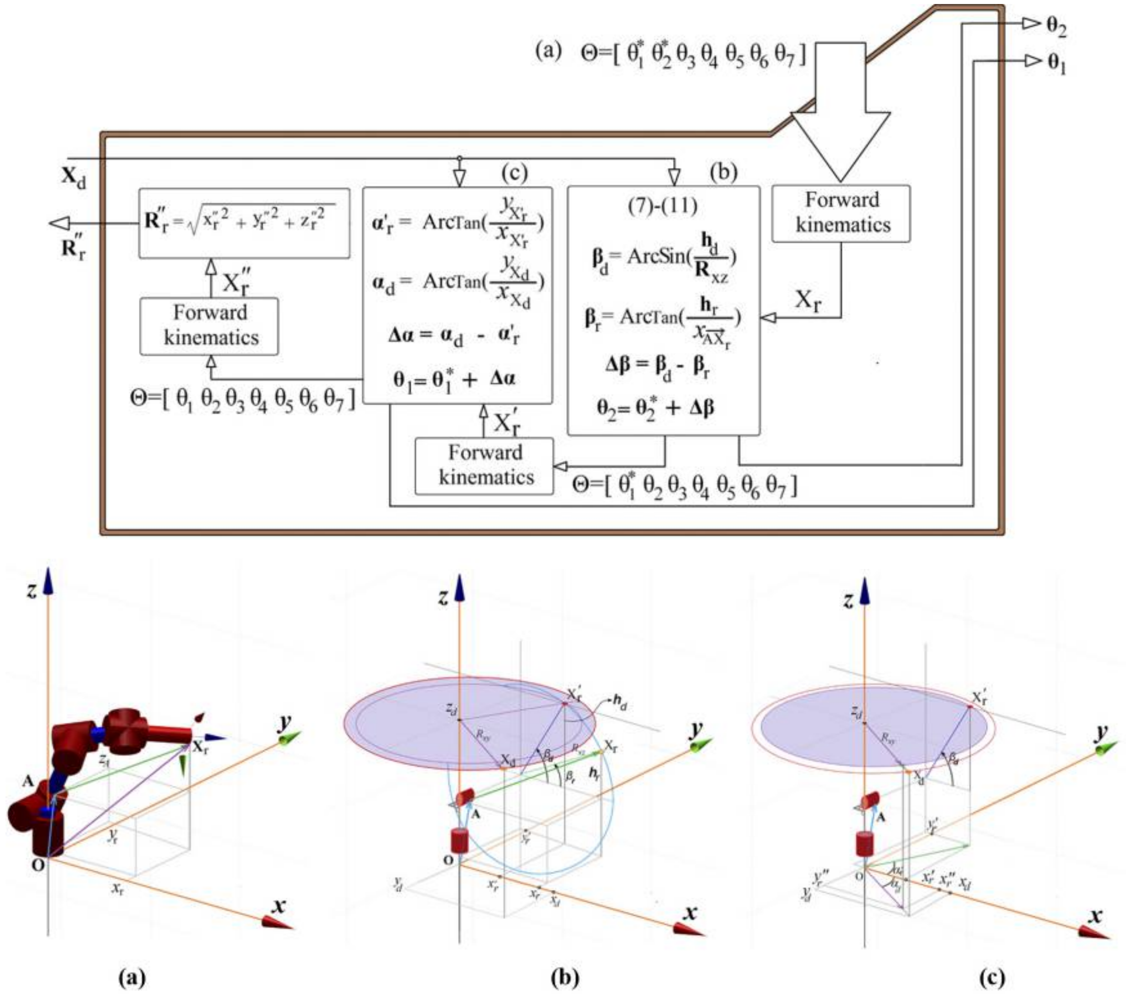
(a) $\Theta=[\theta_1^* \theta_2^* \theta_3 \theta_4 \theta_5 \theta_6 \theta_7]$
$\theta_2$
$\theta_1$
$X_d$
(c)
(b)
$R''_r = \sqrt{x_r''^2 + y_r''^2 + z_r''^2}$
$R''_r$
$X''_r$
Forward kinematics
$\Theta=[\theta_1 \theta_2 \theta_3 \theta_4 \theta_5 \theta_6 \theta_7]$
$\alpha'_r = \mathrm{ArcTan}(\frac{y_{X_r}}{x_{X_r}})$
$\alpha_d = \mathrm{ArcTan}(\frac{y_{X_d}}{x_{X_d}})$
$\Delta\alpha = \alpha_d - \alpha'_r$
$\theta_1 = \theta_1^* + \Delta\alpha$
$X'_r$
Forward kinematics
(7)-(11)
$\beta_d = \mathrm{ArcSin}(\frac{h_d}{R_{xz}})$
$\beta_r = \mathrm{ArcTan}(\frac{h_r}{x_{AX_r}})$
$\Delta\beta = \beta_d - \beta_r$
$\theta_2 = \theta_2^* + \Delta\beta$
Forward kinematics
$X_r$
$\Theta=[\theta_1^* \theta_2 \theta_3 \theta_4 \theta_5 \theta_6 \theta_7]$
z
y
x
A
O
$X_r$
$z_r$
$y_r$
$x_r$
$X'_r$
$h_d$
$z_d$
$X_d$
$\beta_d$
$\beta_r$
$h_r$
$y_d$
$x_d$
$X''_r$
$\Delta\alpha$
(a)
(b)
(c)

**Notes:** (a) 7DOFs manipulator with a spatial positioning of the end-effector. (b) positioning of the end-effector on the desired height $h_d$ requiring to relocate the second joint from angle $\beta_r$ to $\beta_d$. (c) first joint rotated as $\Delta\alpha = \alpha_d - \alpha'_r$ in order to be aligned with the target point $X_d$ (violet line)

the predicted joint profiles for the given trajectory. In this figure, four polynomial functions (of order 10) are fitted to the predicted joint angles to provide an analytical formulation for joint profiles. Equation (13) represents the analytical formula of whole joint profiles:

$$\begin{cases} \varphi = [0{:}\pi/180{:}\ 276 \ * \ (\pi/180)] \\ x = [0.38{:}\ -8.3333 \times 10^{-4}{:}\ 0.15] \\ y = (0.1 Sin(\varphi)) \\ z = 0.45 + (0.2\cos(\varphi)) \end{cases} \tag{12}$$

$$\theta_j(t) = \sum_{i=0}^{9} P_{i,j} T^i(t);\ j \in [1,\ 2,\ 3,\ 4] \tag{13}$$

To explore the effect of the synergy coefficient on positioning the end effector, we ran the program for a range of values for second synergy coefficient $K_h \in [0.1, 0.9]$. Meanwhile, the coefficient of first synergy is kept equal to 1 to assure that this synergy has a higher coefficient value (because it feeds the even joints). The top graph in Figure 21 shows the RMSE values of each run plotted for various $K_h$ values; bottom graph shows the $K_h$ value with highest accuracy (lowest RMSE). The top graph in Figure 21 depicts the facts that by increasing the contribution of second synergy, the accuracy of algorithm predictions will decrease. Accordingly and also by considering Figure 14 (c), the torsion would endangered the positioning accuracy of end effector. The lower graph shows the synergy coefficients which results in minimum RMSE.

A 3D R letter-shape trajectory is designed to show that the algorithm can work even in near singular positions. For this purpose, we plotted the manipulability measure (14) – which stands for Jacobian determinant of redundant robotic arms – for this trajectory (Figure 22). The graph shows that the algorithm works well in near singular points, and the image c on top proves this fact by illustrating a fully stretched posture.

**Figure 19** Optimal point analysis for 3D oval-shape trajectory. The optimal step size and optimal MAE would be 7.5 × $10^{-4}$ and 1.47 × $10^{-4}$ respectively

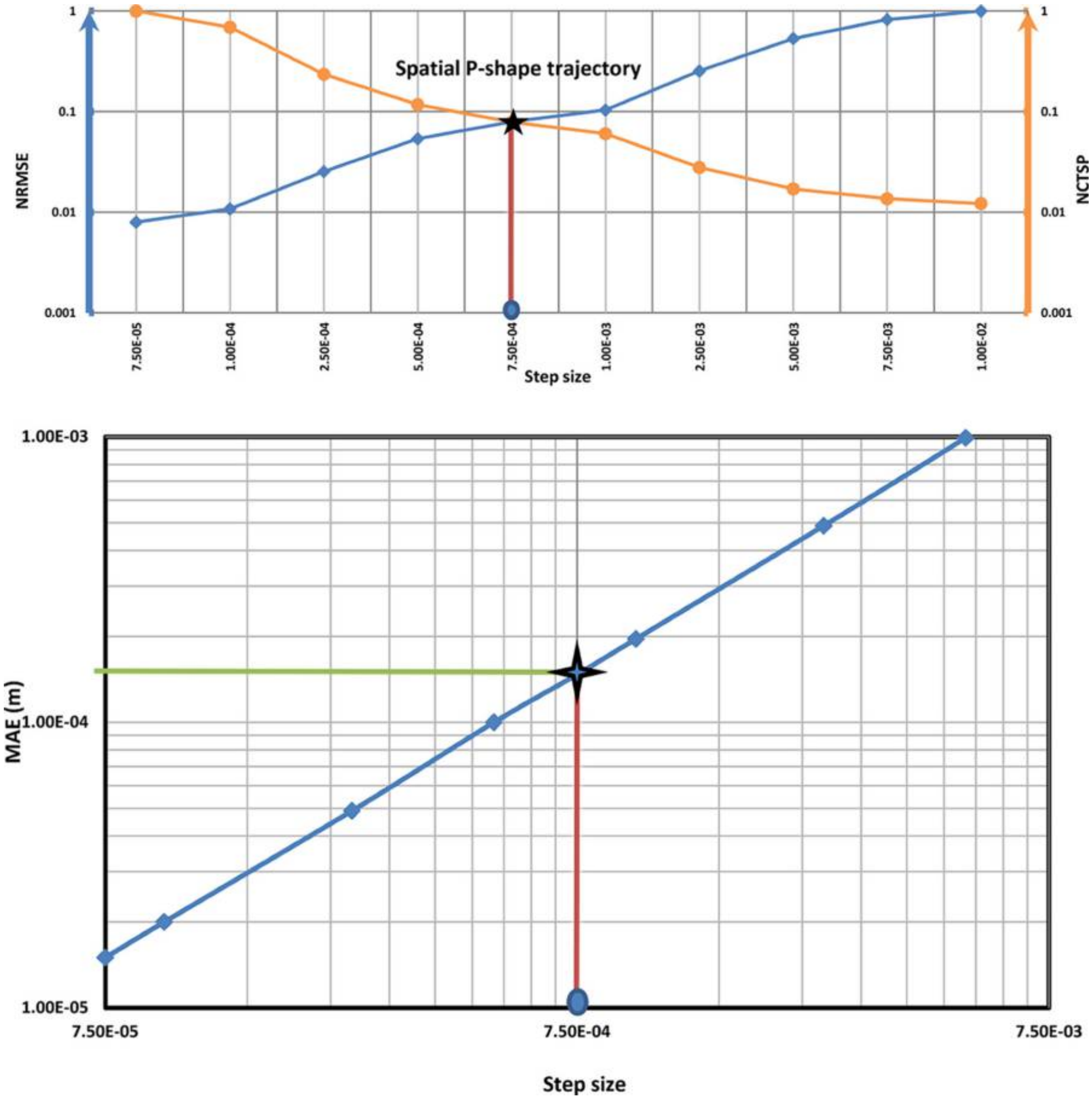

In Figure 22, the position error of the end effector is also plotted together with manipulability index to present the behavior of end effector among trajectory and specifically in near singular point:

$$w = \sqrt{\det(\mathfrak{J}(\Theta)\mathfrak{J}(\Theta)^T)} \tag{14}$$

## 5. Discussion and conclusion

The biomimetic motion planning approach is presented in two episodes: the first was a planar motion planning approach and, second, integration in a 3D motion generation algorithm. The prior takes advantage of a 2-DOF simplified non-redundant model of manipulator which is implemented in a feedback control loop (Figure 4) to control the position of end effector in a plane. In fact, the kinematic redundancy provides a potential capability to create various robot structure morphology, so the core idea is to exploit the meaningful morphology which locates robot end effector in a given position.

In the later episode, we took inspiration from the biological concept of postural synergies to introduce two joint groups/synergies that each one creates, i.e. an independent 2D morphology. The human arm movements are considered to design and combine the postural synergies in a way that each synergy follows a anatomical motion. Consequently, the superposition of these two postural synergies would create a curvature which leads to a 3D positioning of end effector. Since each synergy is controlled by an independent parabola, so, just two variables (the curvature values of parabolas) are required for controlling all of the 7 DOFs. In other words, applying the joint synergy concept causes a simplification in controlling the redundant manipulator.

**Figure 20** Joint analytical angle profiles plotted for 3D oval-shaped trajectory

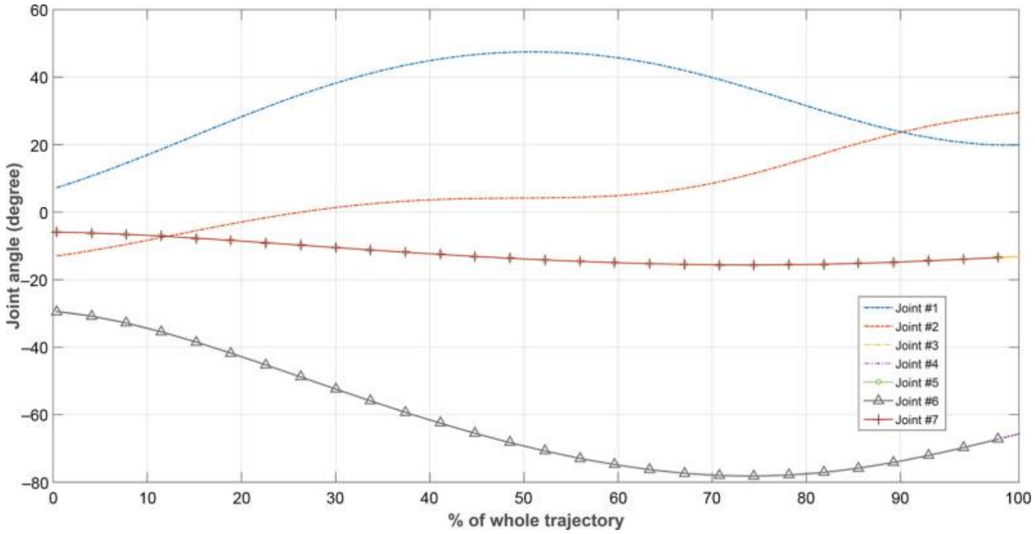

The spatial motion planning algorithm was used to predict the joint angles for a 7-DOF anthropomorphic robotic manipulator following a 3D oval spring. The resulted joint angles presented in Figure 20 illustrate the continuity and smoothness of joint profiles. Because of these two main features, we were able to fit a set of polynomial equation of order 10 over the predicted joint angles which result in an analytical formulation for joint profiles (Table II).

**Figure 21** Top graph: RMSE plotted for tracking 3D oval-shape trajectory with different values of synergy coefficient $\mathbf{K_h}$. Lower graph: zoom-in for area $\mathbf{K_h} \in [0.1, 0.4]$ which depicts $\mathbf{K_h}$ value with minimum **RMSE** value ($\mathbf{K_h} = 0.2$)

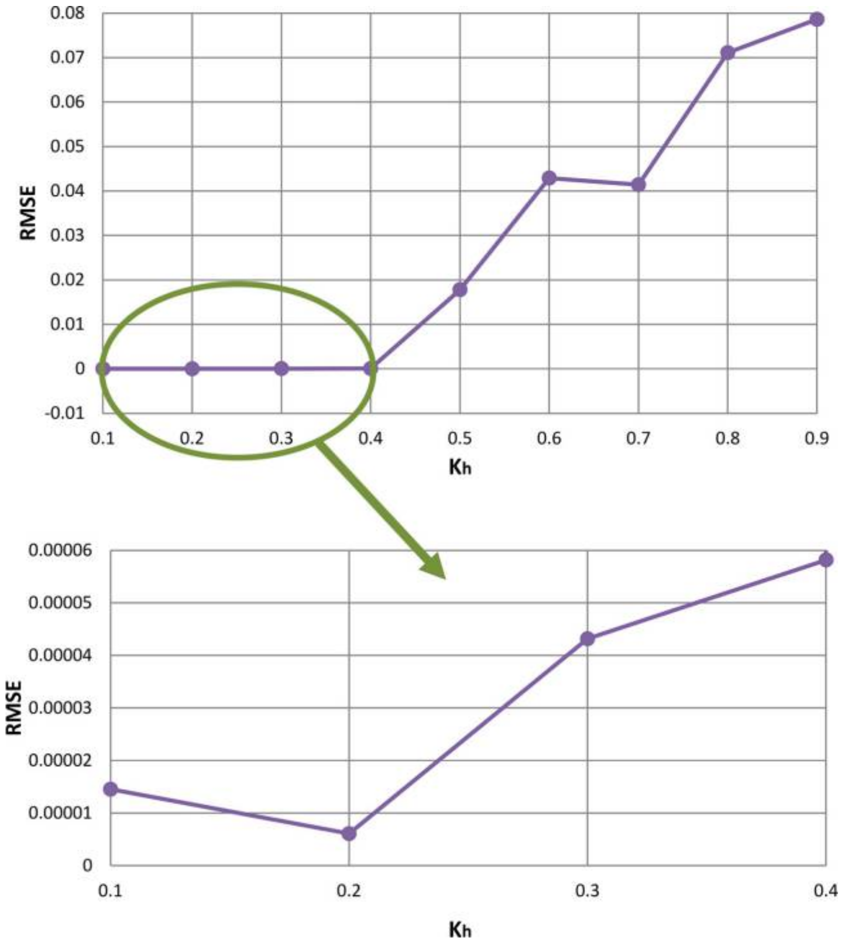

**Table II.** Values of polynomial coefficients for joint angle profiles

| Joint no. | P0 | P1 | P2 | P3 | P4 | P5 | P6 | P7 | P8 | P9 |
|---|---|---|---|---|---|---|---|---|---|---|
| 1 | 4.93E-21 | −6.49E-18 | 3.55E-15 | −1.04E-12 | 1.79E-10 | −1.79E-08 | 1.07E-06 | −6.00E-05 | 0.003425872 | 0.308168582 |
| 2 | −9.87E-21 | 1.31E-17 | −7.20E-15 | 2.14E-12 | −3.74E-10 | 3.99E-08 | −2.51E-06 | 6.86E-05 | 0.000495263 | 0.144486011 |
| 3, 5, 7 | 1.11E-23 | 2.79E-20 | −4.11E-17 | 2.05E-14 | −5.21E-12 | 7.67E-10 | −7.89E-08 | 9.15E-06 | −0.000967951 | −0.016354665 |
| 4, 6 | 5.53E-23 | 1.40E-19 | −2.05E-16 | 1.03E-13 | −2.60E-11 | 3.83E-09 | −3.94E-07 | 4.58E-05 | −0.004839756 | −0.081773326 |

Furthermore, by designing time function $T(t)$ in equation (14), we can manage the velocity of predicted motion. It is worth mentioning that the considered mechanism in planar motion planning, given in Figure 17, has three DOFs with equal length of linkages and it follows a parabolic curve, so, inevitably, the predicted angles for second and third joints may have been the same. Accordingly, the profiles of third and fourth joints have the same trend of fifth, sixth and seventh joints because those are commanded by $q_2$ and $q_3$ (Figure 17).

We designed a more complex trajectory for end effector to analyze the algorithm in terms of singularity and tracking behavior. The path is designed as "R" letter shaped to embed both direct lines (vertical and diagonal) and curves and it is positioned as far as possible from robot (in a way that a part of trace would be on the boundary of robot's workspace). The manipulability measure in Figure 22 decreases as end effector's distance (from the origin) increases and in the point c has its minimum value. The c is a point close to singularity, as the value of manipulability measure is almost zero which intuitively can be seen in snapshot c (whole joints are aligned). The singularity at the point c also causes a change in sign of end effector's position error.

**Figure 22** Upper graph: robot configurations during tracking an "**R**" letter-shaped trajectory: middle graph: position error of the end-effector; lower graph: equivalent manipulability measure during the trajectory tracking

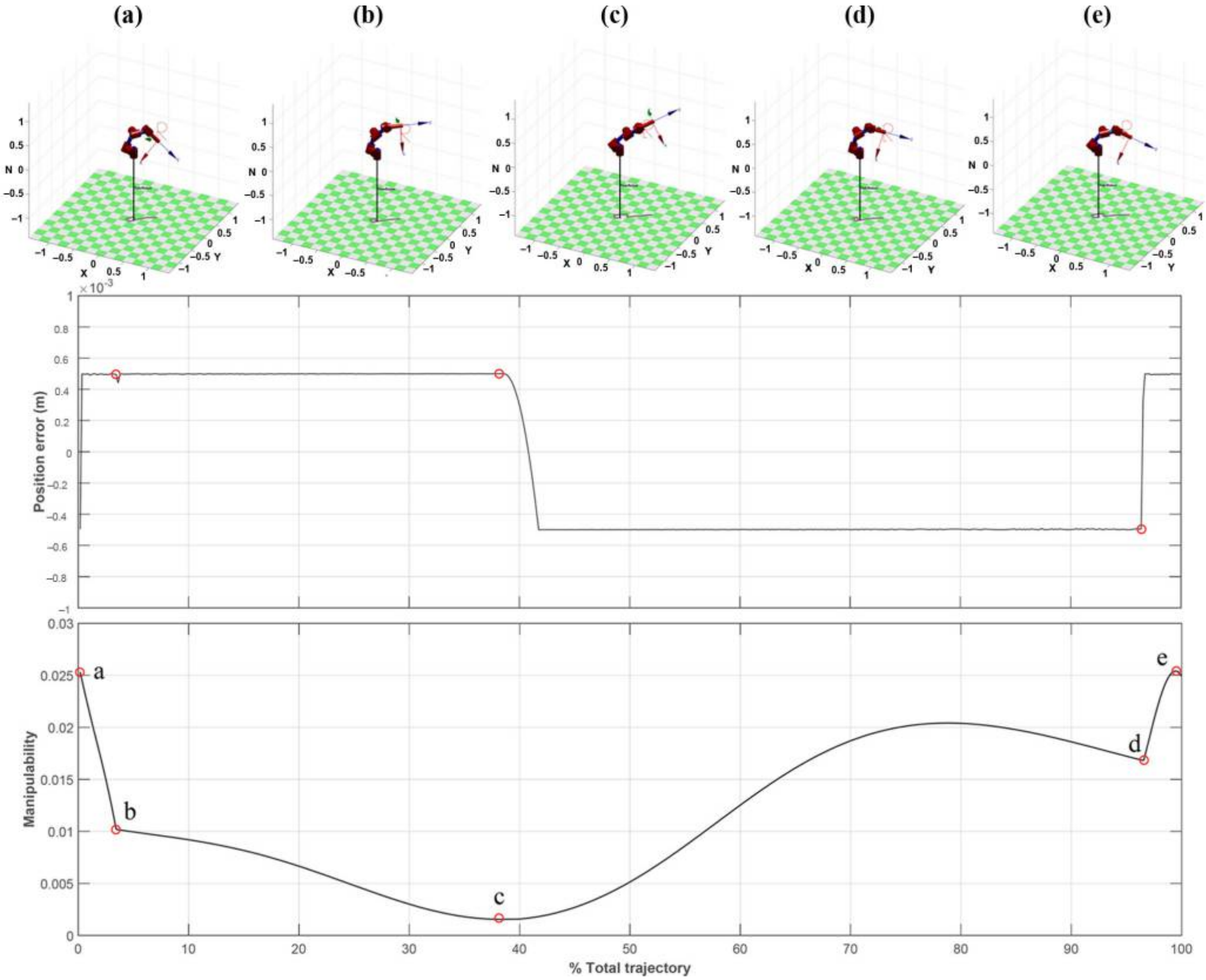

The simulation results (Figures 8 and 9 for planar robot and Figure 20 for spatial manipulator) illustrate that the posture of robot varies continuously with no self-collision, while the end effector strictly follows the predefined planar trajectory. Comparison of the resulting error magnitude (i.e. millimeter) with the robot size (4 meters) convincingly demonstrates that the position error is rather negligible (Figure 10) for planar motion planning. The values of RMSE show the algorithm's stability (Table I). The low computational time for single point (CTSP) values also show that the algorithm can be used for a real-time motion planning (Table I).

The algorithm will not be endangered by kinematic singularities, as it is not using the Jacobian-based solutions for motion planning. The analytical angle–time equations of joints are scalable which allowed us to design a desired velocity for joints to achieve desired dynamic at end-effector level. As the robot's configuration follows a parabolic curve, the self-collision will not happen ever. In summary, singularity free, low computational burden, self-collision avoidance, joint profiles scalability and algorithm stability are the main advantages of the presented approach.

## References

Abedi, P. and Leylavi Shoushtari, A. (2012), "Modelling and simulation of human-like movements for humanoid robots", *Proceedings of 9th International Conference on Informatics in Control, Automation and Robotics (ICINCO) CITEPRESS, Rome, Italy*, pp. 342-346.

Artemiadis, P.K., Katsiaris, P.T. and Kyriakopoulos, K.J. (2010), "A biomimetic approach to inverse kinematics for a redundant robot arm", *Autonomous Robots*, Vol. 29 Nos 3/4, pp. 293-308.

Asuni, G., Leoni, F., Guglielmelli, E., Starita, A. and Dario, P. (2003), "A neuro-controller for robotic manipulators based on biologically inspired visuo-motor co-ordination neural models", *Proceedings of First International IEEE EMBS Conference on Neural Engineering, Capri Island, Italy*, pp. 450-453.

Asuni, G., Teti, G., Laschi, C., Guglielmelli, E. and Dario, P. (2006), "Extension to end-effector position and orientation control of a learning-based neurocontroller for a humanoid arm", *Proceedings of the 2006 IEEE/RSJ International Conference on Intelligent Robots and Systems, Beijing, China*, pp. 4151-4156.

Caggiano, V., De Santis, A., Siciliano, B. and Chianese, A. (2006), "A biomimetic approach to mobility distribution for a human-like redundant arm", *Proceedings of the IEEE/RAS-EMBS International Conference on Biomedical Robotics and Biomechatronics, Pisa, Italy*, pp. 393-398.

Chang, P.H. (1987), "A closed-form solution for inverse kinematics of robot manipulators with redundancy", *IEEE Transactions on Robotics and Automation*, Vol. 3 No. 5, pp. 393-403.

Chen, T.H., Cheng, F.T., Sun, Y.Y. and Hung, M.H. (1994), "Torque optimization schemes for kinematically redundant manipulators", *Journal of Robotic Systems*, Vol. 11 No. 4, pp. 257-269.

Chiaverini, S. (1997), "Singularity-robust task-priority redundancy resolution for real-time kinematic control of robot manipulators", *IEEE Transactions on Robotics and Automation*, Vol. 13 No. 3, pp. 398-410.

Cruse, H., Wischmeyer, E., Bruser, M., Brockfeld, P. and Dress, A. (1990), "On the cost functions for the control of the human arm movement", *Biological Cybernetics*, Vol. 62 No. 6, pp. 519-528.

Guglielmelli, E., Asuni, G., Leoni, F., Starita, A. and Dario, P. (2006), "Neurocontroller for Robot arms based on biologically inspired visuomotor coordination neural models", in Akay, M. (Ed.), *Handbook of Neural Engineering*, John Wiley & Sons, Hoboken, NJ, pp. 433-448.

Hollerbach, J.M. and Suh, K. (1987), "Redundancy resolution of manipulators through torque optimization", *IEEE Journal on Robotics and Automation*, Vol. 3 No. 4, pp. 308-316.

Khatib, O., Demircan, E., De sapio, V., Sentis, L., Besier, T. and Delp, S. (2009), "Robotics-based synthesis of human motion", *Journal of Physiology-Paris*, Vol. 103 Nos 3/5, pp. 211-219.

Kim, C., Kim, D. and Oh, Y. (2005), "Solving an inverse kinematics problem for a humanoid robot's imitation of human motions using optimization", in *Proceedings of the Second International Conference on Informatics in Control, Automation and Robotics*, ISBN 972-8865-30-9, pp. 85-92. DOI: 10.5220/0001180100850092.

Leylavi Shoushtari, A. (2013), "What strategy central nervous system uses to perform movement balanced? Biomechatronical simulation of human lifting", *Applied Bionics and Biomechanics*, Vol. 10 Nos 2/3, pp. 113-124.

Maciejewski, A.A. and Klein, C.A. (1985), "Obstacle avoidance for kinematically redundant manipulators in dynamically varying environments", *International Journal of Robotic Research*, Vol. 4 No. 3, pp. 109-117.

Nakamura, Y., Hanafusa, H. and Yoshikawa, T. (1987), "Task-priority based redundancy control of robot manipulators", *International Journal of Robotic Research*, Vol. 6 No. 2, pp. 3-15.

Palli, G., Melchiorri, C., Vassura, G., Scarcia, U., Moriello, L., Berselli, G. and Siciliano, B. (2014), "The DEXMART hand: mechatronic design and experimental evaluation of synergy-based control for human-like grasping", *The International Journal of Robotics Research*, Vol. 33 No. 5, pp. 799-824.

Pollard, N.S., Hodgins, J.K., Riley, M.J. and Atkeson, C.G. (2002), "Adapting human motion for the control of a humanoid robot", *Proceedings of IEEE International Conference on Robotics and Automation*, Vol. 2, pp. 1390-1397.

Potkonjak, V., Popovic, M., Lazarevic, M. and Sinanovic, J. (1998), "Redundancy problem in writing: from human to anthropomorphic robot arm", *IEEE Transaction on Systems, Man and Cybernetics, Part B*, Vol. 28 No. 6, pp. 790-805.

Qiao, H., Li, C., Yin, P., Wu, W. and Liu, Z.Y. (2015), "Human-inspired motion model of upper-limb with fast response and learning ability: a promising direction for robot system and control", *Assembly Automation*, Vol. 36 No. 1.

Ramos, M.C. and Koivo, A.J. (2002), "Fuzzy logic based optimization for redundant manipulators", *IEEE Transactions on Fuzzy Systems*, Vol. 10 No. 4, pp. 498-509.

Santello, M., Flanders, M. and Soechting, J.F. (1998), "Postural hand synergies for tool use", *The Journal of Neuroscience*, Vol. 18 No. 23, pp. 10105-10115.

Seraji, H. (1989), "Configuration control of redundant manipulators: theory and implementation", *IEEE Transactions on Robotics and Automation, Autom.*, Vol. 5 No. 4, pp. 472-490.

Siciliano, B. (1990), "Kinematic control of redundant robot manipulators: a tutorial", *Journal of Intelligent and Robotic Systems*, Vol. 3 No. 3, pp. 201-212.

Suarez, R., Rosell, J. and Garcia, N. (2015), "Using synergies in dual-arm manipulation tasks", *Proceedings of IEEE International Conference on Robotics and Automation (ICRA), Seattle, WA*, pp. 5655-5661.

Torres-Oviedo, G., Macpherson, J.M. and Ting, L.H. (2006), "Muscle synergy organization is robust across a variety of postural perturbations", *Journal of Neurophysiology*, Vol. 96 No. 3, pp. 1530-1546.

Wang, J. (1997), "Recurrent neural networks for computing pseudo-inverses of rank-deficient matrices", *Siam Journal on Scientific Computing*, Vol. 18 No. 5, pp. 1479-1493.

Whitney, D.E. (1969), "Resolved motion rate control of manipulators and human prostheses", *IEEE Transactions on Man-Machine Systems*, Vol. 10 No. 2, pp. 47-53.

Whitney, D.E. (1972), "The mathematics of coordinated control of prosthetic arms and manipulators", *Journal of Dynamic Systems Measurement and Control*, Vol. 94 No. 4, pp. 303-309.

Xia, Y. (1966), "A new neural network for solving linear programming problems and its application", *IEEE Transactions on Neural Networks*, Vol. 7 No. 2, pp. 525-529.

Yoshikawa, T. (1985), "Manipulability of robotic mechanisms", *International Journal of Robotics Research*, Vol. 4 No. 2, pp. 3-9.

## Corresponding author

**Ali Leylavi Shoushtari** can be contacted at: a.leylavishoushtari@sssup.it